Acta Pharmaceutica Sinica B 2021;11(7):1853−1866

Chinese Pharmaceutical Association
Institute of Materia Medica, Chinese Academy of Medical Sciences

Acta Pharmaceutica Sinica B

www.elsevier.com/locate/apsb
www.sciencedirect.com

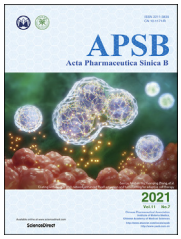

ORIGINAL ARTICLE

Pharmacologically targeting molecular motor promotes mitochondrial fission for anti-cancer

Yi Qian[a,†], Meimei Zhao[a,†], Qinghua Han[a], Jingkang Wang[a], Lixi Liao[a], Heng Yang[a], Dan Liu[b], Pengfei Tu[a], Hong Liang[a,*], Kewu Zeng[a,*]

[a]*State Key Laboratory of Natural and Biomimetic Drugs, School of Pharmaceutical Sciences, Peking University, Beijing 100191, China*
[b]*Proteomics Laboratory, Medical and Healthy Analytical Center, Peking University Health Science Center, Beijing 100191, China*

Received 15 September 2020; received in revised form 26 November 2020; accepted 1 December 2020

KEY WORDS

Anti-cancer;
Liver hepatocellular carcinoma;
Mitochondrial fission;
Small molecule;
Target identification;
Molecular motor;
MYH9;
HSPA9

Abstract Mitochondrial shape rapidly changes by dynamic balance of fusion and fission to adjust to constantly changing energy demands of cancer cells. Mitochondrial dynamics balance is exactly regulated by molecular motor consisted of myosin and actin cytoskeleton proteins. Thus, targeting myosin−actin molecular motor is considered as a promising strategy for anti-cancer. In this study, we performed a proof-of-concept study with a natural-derived small-molecule J13 to test the feasibility of anti-cancer therapeutics *via* pharmacologically targeting molecular motor. Here, we found J13 could directly target myosin-9 (MYH9)−actin molecular motor to promote mitochondrial fission progression, and markedly inhibited cancer cells survival, proliferation and migration. Mechanism study revealed that J13 impaired MYH9−actin interaction to inactivate molecular motor, and caused a cytoskeleton-dependent mitochondrial dynamics imbalance. Moreover, stable isotope labeling with amino acids in cell culture (SILAC) technology-coupled with pulldown analysis identified HSPA9 as a crucial adaptor protein connecting MYH9−actin molecular motor to mitochondrial fission. Taken together, we reported the first natural small-molecule directly targeting MYH9−actin molecular motor for anti-cancer translational research.

Abbreviations: CAM, chick embryo chorioallantoic membrane; CETSA, cellular thermal shift assay; Co-IP, co-immunoprecipitation; DAPI, 4′,6-diamidino-2-phenylindole; ER, endoplasmic reticulum; HE, hematoxylin−eosin staining; HSPA9, heat-shock protein A9; HUVEC, human umbilical vein endothelial cells; IHC, immunohistochemistry; LIHC, liver hepatocellular carcinoma; MMP, mitochondrial membrane potential; MYH9, myosin-9; SILAC, stable isotope labeling with amino acids in cell culture; SPR, surface plasmon resonance; TUNEL, terminal deoxynucleotidyl transferase-mediated dUTP nick-end labeling.

*Corresponding authors.
E-mail addresses: lianghong@bjmu.edu.cn (Hong Liang), ZKW@bjmu.edu.cn (Kewu Zeng).
[†]These authors made equal contributions to this work.

Peer review under responsibility of Chinese Pharmaceutical Association and Institute of Materia Medica, Chinese Academy of Medical Sciences.

https://doi.org/10.1016/j.apsb.2021.01.011

2211-3835 © 2021 Chinese Pharmaceutical Association and Institute of Materia Medica, Chinese Academy of Medical Sciences. Production and hosting by Elsevier B.V. This is an open access article under the CC BY-NC-ND license (http://creativecommons.org/licenses/by-nc-nd/4.0/).

Besides, our study also proved the conceptual practicability of pharmacologically disrupting mitochondrial fission/fusion dynamics in human cancer therapy.

© 2021 Chinese Pharmaceutical Association and Institute of Materia Medica, Chinese Academy of Medical Sciences. Production and hosting by Elsevier B.V. This is an open access article under the CC BY-NC-ND license (http://creativecommons.org/licenses/by-nc-nd/4.0/).

1. Introduction

Mitochondria are crucial organelles to produce energy for efficient maintenance of cell functions[1,2]. Mitochondria possess capability of changing self-morphology, which is called mitochondrial dynamics, in response to external dangerous stimuli including oxidative stress, nutrient deprivation, UV radiation, and toxic chemicals[3,4]. Mitochondrial dynamics is regulated by two opposed processes: mitochondrial fission and fusion, which are well conserved between mammals, flies and yeast[5]. Appropriate fission/fusion dynamics is critical to maintain mitochondrial homeostasis, and is accurately controlled in cells[6,7]. Mitochondrial fission plays a key role in mitochondrial movement to the regions that lack of energy by forming smaller fragmented mitochondria. Meanwhile, mitochondria tend to fuse together under damaged condition to share nutrients and genetic mtDNA for preserving normal oxidative phosphorylation and ATP energy supply[8]. Dysregulation of mitochondrial fission/fusion process is widely implicated in various cell stresses, and seriously affects mitochondrial quality control, which has been linked to various human diseases especially for cancers[9−12].

Nowadays, specifically targeting mitochondrial dynamics has become an attractive issue in cancer therapy[13]. A consensus has emerged that increased mitochondrial fission is a pro-tumorigenic phenotype. Thus, inhibition of mitochondrial fission has been considered as a potential strategy for cancer treatment[10,11,14−17]. However, limited attempts have been reported so far in clinical studies, implying a potential high risk and uncertainty of this anticancer strategy. Curiously, it has been recently reported that an excess of fission promotes mitochondrial dysfunction, which may play an unfavorable role in cancer cell growth[18]. Therefore, pharmacological induction of mitochondrial fission could provide novel insight into anti-cancer therapy, but this concept has not yet been adequately validated.

Currently, mitochondrial fission/fusion dynamics modulation mechanism has not been widely clarified[19]. Accumulating evidence show that molecular motor proteins are master regulators powering mitochondrial dynamics in living organisms[20,21]. Of note, myosin is a crucial molecular motor protein that slides along actin filaments by utilizing energy from ATP hydrolysis[22]. Previous report suggests that myosin and actin could form archetypical molecular motor complex to regulate mitochondria fission/fusion dynamics, morphology and cellular localization[23,24]. Genetic downregulation of myosin markedly suppresses mitochondrial fission to promote elongated mitochondria number[25]. Intriguingly, it has been also found that mitochondrial fission occurs at mitochondria-endoplasmic reticulum (ER) contact sites with F-actin accumulation, which drives dynamin-related protein DRP1 recruitment to fuel mitochondrial fission[26]. Therefore, it is significant to explore potential strategy for regulating mitochondrial fission *via* targeting myosin−actin molecular motor[24].

In this study, we discovered a natural-derived small-molecule J13 from medicinal plant *Ablizia julibrissin* with obvious anti-hepatoma carcinoma effects *in vitro* and *in vivo* by directly targeting myosin-9 (MYH9)−actin molecular motor. Further investigation showed that J13 bound to actin-binding motif in MYH9 to impair MYH9 interaction with actin and induced molecular motor dysfunction for mitochondrial fission progression. Moreover, heat-shock protein A9 (HSPA9) was identified as a critical substrate protein of MYH9−actin molecular motor for modulating mitochondrial fission. In addition, high expressions of MYH9 and HSPA9 were associated with poor progression and prognosis in liver hepatocellular carcinoma (LIHC). Collectively, for the first time, our proof-of-concept study revealed that J13 was a novel molecule template for regulating molecular motor function. Moreover, MYH9−actin molecular motor may represent a promising pharmacological therapeutic target of mitochondrial dynamics-related diseases especially for human cancers.

2. Materials and methods

2.1. Chemicals and reagents

Julibraside J13 was previously separated and purified from *Ablizia julibrissin* by our laboratory[27], and the purity is above 98% by HPLC analysis. Fatty acid-free bovine serum albumin (BSA) was purchased from Equitech-Bio (Kerrville, TX, USA). 3-[4,5-Dimethylthiazol-2-yl] 2,5-diphenyltetrazolium bromide (MTT) and recombinant actin and myosin heavy chain were obtained from Sigma Chemical (Santa Clara, CA, USA). TransDetect Annexin V-FITC/PI cell kit was obtained from Transgene (Beijing, China). Hoechst 33258 staining kit and mitochondrial membrane potential assay kit were obtained from Beyotime (Nanjing, China). Fetal bovine serum (FBS) was from PAN-Biotech (Logan, UT, USA). High glucose Dulbecco's modified Eagle's medium (DMEM, 4.5 g/L glucose), antibiotics and trypsin were from Macgene (Beijing, China). Primary antibodies and secondary antibodies were from Cell Signaling Technology (Beverly, MA, USA). Chemiluminescent HRP substrate was purchased from Thermo Scientific (Waltham, MA, USA).

2.2. Methods

2.2.1. Cell culture

Human hepatoma cell lines (HepG2/Hepa1-6/Bel7402/SMMC7721), human umbilical vein endothelial cells (HUVEC), human embryonic kidney 293 cells (HEK293) and mouse hepatoma cell line (H22) were obtained from the State Key Laboratory of National and Biomimetic Drugs, Peking University Health Science Centre (Beijing, China), and cultured in DMEM supplemented with 10% FBS, 100 U/mL streptomycin at 37 °C in a humidified incubator with 95% air and 5% CO_2.

2.2.2. Plasmids and siRNA

The plasmids of *HA-MYH9*, *His-HSPA9*, *MYH9 F* (83−764 aa) and *MYH9 M* (del 654−676 aa) were constructed by Biogot

Technology (Nanjing, China). Specific *MYH9* siRNAs were designed and synthesized at GenePharma (Shanghai, China) as listed in Supporting Information Table S1. The indicated plasmids or siRNA were transfected into HepG-2 cells using Lipofectamine 2000 (Invitrogen, Waltham, CA, USA) or Lipofectamine RNAiMAX (Thermo Scientific, Waltham, MA, USA) respectively. After 48 h, cells were collected for further experiments.

2.2.3. *Cell viability assay*

Cell viability was detected *via* colorimetric MTT assay. After treatment, MTT solutions (5 mg/mL) were added to each well. After incubation for 2 h, supernatants were aspirated and formazan crystals were dissolved in DMSO. The amount of purple formazan was assessed by measuring the absorbance at 570 nm using Infinite F50 Absorbance Microplate Reader (Tecan, Mannedorf, Switzerland).

2.2.4. *Hoechst 33258 staining assay*

Hoechst 33258 staining assay was used to visualize nuclear change and apoptotic body formation. After treatment, cells were washed with PBS and fixed with 4% formaldehyde at 4 °C for 20 min. The fixing solution was removed and cells were washed twice with PBS before staining with Hoechst 33258 (5 μg/mL). After 5 min, cells were washed and observed under a fluorescence microscope (IX73, Olympus, Tokyo, Japan) with excitation at 360 nm and emission at 460 nm.

2.2.5. *Terminal deoxynucleotidyl transferase-mediated dUTP nick-end labeling (TUNEL) assay*

TUNEL assay kit (Life, Waltham, MA, USA) was employed to quantify DNA strand breaks in apoptosis. Briefly, after deparaffinization, rehydration, permeabilization and blocking, tumor tissues or HepG2 cells were incubated with TUNEL reaction mixture at 37 °C for 1 h in a humid and dark condition. For staining of nuclei, cells were treated with 4′,6-diamidino-2-phenylindole (DAPI) for 15 min at room temperature. After washing with PBS, tissue or cell samples were imaged by an IX73 fluorescence microscope (Olympus, Tokyo, Japan). DAPI was visualized at 358 nm (excitation) and 460 nm (emission). FITC was visualized at 488 nm (excitation) and 516 nm (emission). Percentage of number of TUNEL-positive cells (green) to total cells (DAPI-positive cells, blue) was calculated as the percentage of apoptotic cells.

2.2.6. *Mitochondrial membrane potential (MMP) analysis*

After treatment, cells were incubated with 10 μg/mL JC-1 solution for 20 min at 37 °C. Then, cells were washed and observed with the Olympus IX73 fluorescence microscope (Olympus, Tokyo, Japan). Green fluorescence was detected with 488 nm (excitation) and 525 nm (emission) filters, whereas red fluorescence was visualized with 488 nm (excitation) and 590 nm (emission) filters.

2.2.7. *Preparation of J13-tagged beads*

Epoxy-actived Sepharose 4B beads (GE Healthcare, Chicago, IL, USA) were added into stilled water and left overnight to allow beads completely swelled. Beads were then incubated with J13 or solvent for 12 h under constant rotation at 37 °C. After remove of supernatants through centrifugation at 3000 rpm (6380R, Eppendorf, Hamburg, Germany) for 2 min, residual active sites were quenched using ethanolamine solution (1 mol/L, pH 8.5) for 2 h with agitation. J13-tagged beads were washed with stilled water and stored at 4 °C until further use.

2.2.8. *Cellular target identification of J13*

Cell lysates were incubated with J13-tagged beads at 4 °C for 12 h. Meanwhile, an excess amount of J13 for competition was added into lysates. Target proteins were specifically bound to J13-tagged beads and then eluted by boiling in SDS-loading buffer for 10 min. Supernatants were obtained and subjected to SDS-PAGE followed by silver staining. The bands with obvious difference upon J13 treatment were separated, trypsin-digested and identified by LC−MS/MS analysis as described in our previous publication[28].

2.2.9. *Cellular thermal shift assay (CETSA)*

Cells were collected and freeze-thawed three times using liquid nitrogen. Cell suspensions were divided into 2 aliquots and treated with or without J13 (5 μmol/L) for 1 h at room temperature. Each aliquot was heated at indicated temperature (38−64 °C) for 3 min followed by cooling for 3 min. Supernatants were isolated and analyzed by Western blot. Additionally, for living cell CETSA experiment, cells were treated with or without J13 (5 μmol/L) for 6 h, harvested, and heated separately at indicated temperature (38−64 °C) followed by 3 min cooling. Cells were collected and freeze-thawed three times using liquid nitrogen. Supernatants were analyzed by Western blot.

2.2.10. *Surface plasmon resonance (SPR) assay*

SPR measurement was performed on Biocore T200 system (GE Healthcare, Boston, USA) using a carboxymethylated 5 sensor chip. Recombinant MYH9 and β-actin proteins were dissolved in running buffer (Tris−HCl 50 mmol/L, pH 7.2, 100 mmol/L KCl). Protein samples were immobilized on chip *via* amine coupling chemistry in 10 mmol/L sodium acetate at pH 4.5. Ligand solutions were injected as analytes. Data were analyzed with Biocore evaluation software (T200 Version 2.0) using 1:1 langmuir model to fit kinetic data.

2.2.11. *Tryptophan fluorescence quenching assay*

Recombinant MYH9 and β-actin proteins were diluted to 500 μmol/L with PBS, and mixed with gradient concentration of J13 (0.39−100 μmol/L). Tryptophan fluorescence was monitored with λ_{ex} 278 nm and λ_{em} 300−500 nm at 1 nm increment on the PerkinElmer fluorescence spectrophotometer (PerkinElmer EnSpire, Waltham, MA, USA). Fluorescence intensities were corrected by buffer contribution.

2.2.12. *Co-immunoprecipitation (co-IP) analysis*

For co-IP analysis, protein lysates of HepG2 cells were treated with protein A/G agarose for 1 h at 4 °C and centrifuged to obtain supernatants. Samples were incubated with specific primary antibodies at 4 °C overnight and subsequent protein A/G agarose beads for 4 h at 4 °C. Beads were centrifuged and washed five times with IP buffer (0.01% Triton X-100). The immunoprecipitated proteins were eluted by boiling in SDS-loading buffer for 10 min. Final eluate was subjected to SDS-PAGE and analyzed by Western blot.

2.2.13. *Molecular docking analysis*

Three-dimensional structure of J13 was built in Open Babel software. Since X-ray crystal structures of human β-actin and MYH9 have not been reported, we searched for Protein Data Bank (PDB) (http://www.ncbi.nlm.nih.gow/protein/) to find a proper structural template for homology modeling. We used crystal structure of human α-actin (PDB ID code: 5JLH, chain A) and

human MYH14 (PDB ID code: 5JLH, chain F) as input. Homology model was generated in SWISS-MODEL web server as the receptor model in docking stimulation. J13 was placed into the indicated cave which was identified in our study during molecular docking procedure. All calculations were carried out using Autodock Vina software, and Pymol software was used to analyze interaction types of docked proteins with ligand.

2.2.14. Actin polymerization assay

G-actin (200 μg/mL) was mixed with Tris−HCl (pH 8.0), 2 μmol/L FITC-phalloidin methanol solution, 20 mmol/L ATP and different concentrations of J13 (0−0.1 μmol/L). Reaction was started by adding actin polymerization solution (50 mmol/L KCl, 1 mmol/L $MgCl_2$), and continuously detected on the PerkinElmer fluorescence spectrometer (PerkinElmer EnSpire, Waltham, MA, USA) for 15 min (λ_{ex} 545 nm, λ_{em} 570 nm).

2.2.15. Immunofluorescence and morphological staining

For immunofluorescence staining of G-actin, HSPA9 and COX IV, cells were fixed with 4% paraformaldehyde and permeabilized with 0.5% Triton X-100. After blocking with 1% BSA in PBS for 20 min, cells were incubated with primary antibodies at 4 °C overnight. After incubation, cells were incubated with anti-rabbit IgG Alexa Fluor 488 or anti-mouse IgG Alexa Fluor 594 for 1 h at room temperature. Nuclei were stained with DAPI (50 μg/mL, 358 nm/460 nm) for 15 min at room temperature. For morphological staining of filamentous actin (F-actin), mitochondria and endoplasmic reticulum (ER), cells were permeabilized and blocked as immunofluorescence staining. Then, cells were incubated with actin−tracker Green (5 μmol/L, 496 nm/516 nm), Mito−tracker Green (200 nmol/L, 490 nm/516 nm) or ER−tracker Red (1 μmol/L, 504 nm/511 nm), according to the manufacturers' instructions. After being stained with DAPI, cells were imaged on Leica TCS-SP5 confocal laser-scanning microscope (Wetzlar, Germany).

2.2.16. Cell migration assay

Migration assay was carried out using a Transwell with an 8 μm pore size. Briefly, HepG2 cells were seeded onto apical side of Transwell membrane in serum-free medium with or without J13. Medium containing 10% serum was added in basolateral side. Following incubation at 37 °C in 5% CO_2 for 48 h, noninvasive cells were removed by a cotton swab. Membrane containing the migrated cells was fixed with 4% paraformaldehyde for 20 min and stained with 1% crystal violet for 20 min at room temperature. Images were taken in light field by an IX73 fluorescence microscope (Olympus, Tokyo, Japan) and the migrated cells were quantitated with Image J densitometric software.

2.2.17. Tube formation assay

Matrigel (100 μL, Corning, Kennebunk, ME, USA) was added into 96-well plate, and polymerized for 30 min at room temperature. HUVECs were seeded into each well with or without J13. After 6 h incubation, cells were fixed and tube formation was analyzed by an IX73 fluorescence microscope (Olympus, Tokyo, Japan).

2.2.18. Chick embryo chorioallantoic membrane (CAM) assay

Anti-angiogenesis study was evaluated through CAM assay. Windows were cut on egg shells of 8-day-old chick embryos (Vital River, Beijing, China) and resealed with a transparent film to be incubated at 37 °C for further 5 days. During the incubation, J13 or solvent was dropped onto chick embryo chorioallantoic membranes once a day. Then, membranes were fixed with methanol/acetone at ratio of 1:1 for 20 min. Images of the membranes were obtained by an IX73 inverted microscope (Olympus, Tokyo, Japan) and vessel ramification rate was counted by Image J densitometric software.

2.2.19. Western blot assay

Protein samples were separated by SDS-PAGE and transferred onto PVDF membranes. Then, membranes were incubated with primary antibodies at 4 °C for 12 h, followed by incubation with secondary antibody for 1 h at room temperature. Membranes were washed and developed using enhanced chemiluminescence, and detected with Tanon 5200 Imaging Analysis System (Tanon, Shanghai, China).

2.2.20. In vivo anti-tumor studies

2.2.20.1. Animals. Male ICR mice (5−6 weeks old, weight 20−22 g) were obtained from Vital River Laboratories (Beijing, China), and raised in animal house at 25 ± 1 °C under constant dark and light cycles. ICR mice had free access to standard laboratory food and water. All animal experiments were performed under the guidelines of EIACUC-PKU (Ethical Institutional Animal Care and Use Committee of Peking University).

2.2.20.2. Anti-tumor effects evaluation in vivo. After 5 days of acclimatization, H22 cells (1×10^7/mL) were resuspended in saline (0.2 mL) and injected into the flank of ICR mice to form subcutaneous tumor. Five days later, mice were sorted to give different treatments: control-ip (normal saline, intraperitoneal injection), control-ig (normal saline, intragastric administration), J13-ip (0.5, 1.0 and 2.0 mg/kg per day, intraperitoneal injection), J13-ig (1.0, 2.0 and 4.0 mg/kg per day, intragastric administration), and cyclophosphamide (CTX, 30 mg/kg per day, intraperitoneal injection). Animal body weights were measured every day. After 12 days, tumors were weighed, fixed in 4% paraformaldehyde and embedded in paraffin for HE staining and immunohistochemistry (IHC) analysis.

2.3. Statistical analysis

Data were represented as mean ± standard deviation (SD). Statistical analysis was performed by one-way ANOVA with Tukey's multiple comparison post-test. Statistical significance between two groups was performed using Student's *t*-test. A probability value of $P < 0.05$ was considered as statistically significant.

3. Results

3.1. MYH9−actin molecular motor is a direct cellular target of anti-cancer small-molecule J13

To identify effective anti-cancer drugs that might disrupt mitochondrial dynamics, we previously conducted an activity screen of a natural compound library consisting of around 4500 small molecules. Small-molecule J13 was isolated from medicinal plant *Ablizia julibrissin*. MTT assay revealed that J13 exerted obvious anti-hepatoma carcinoma effect in multiple cancer cells (Fig. 1A) but with low toxicity on normal hepatocytes (Supporting Information Fig. S1). We then investigated the mitochondrial morphology change upon J13 treatment. Strikingly, mitochondrial ultrastructure analysis illustrated distorted cristae and many

fragmented mitochondria in response to J13 (Fig. 1B). Moreover, mitochondrial fission was also determined by Mito-tracker staining. As shown in Fig. 1C, J13 obviously caused an increase in mitochondria stained by Mito-tracker from elongated and tubular mitochondria into dots, implicating that mitochondrial morphology shifted towards fission. Inhibition of mitochondrial fission by Mdivi-1 markedly reversed J13-dependent anti-cancer effects, suggesting that mitochondrial fission is involved in J13-induced hepatoma carcinoma HepG2 cell death (Fig. 1D). Mitochondrial dynamics impairment contributes to mitochondrial membrane potential (MMP) decrease. Our findings show that J13 significantly upregulated JC-1 green fluorescence in HepG2 cells (Fig. 1E), reflecting an increase of depolarized mitochondria. In addition, immunofluorescence analysis indicates that J13 promoted mitochondrial fission protein DRP-1 translocation without affecting its expression (Supporting Information Fig. S2A and S2B). Therefore, these observations indicated that J13 exerted anti-cancer activities by potentially promoting mitochondrial fission.

To explore direct cellular target of J13, we prepared J13-coupled agarose beads to capture target proteins from HepG2 cell lysate. Notably, we identified two obvious protein bands (220 kDa for MYH9 and 48 kDa for β-actin) by MS/MS in SDS-PAGE stained with silver (Fig. 1F), which was confirmed by Western blot. Since MYH9 and β-Actin belong to molecular motor proteins, we then used different surfactants (NP40, Triton and SDS) to explore the binding characteristic of J13 to MYH9 and β-actin. As shown in Fig. 1G, rigorous surfactants Triton and SDS obviously inhibited J13 binding to MYH9 and β-actin, but not for weak surfactant NP40, indicating non-covalent bindings of J13 with MYH9 and β-actin. Then surface plasmon resonance (SPR) analysis was performed to show specific bindings of J13 to MYH9 and β-actin (Fig. 1H). Moreover, cellular thermal shift assay (CETSA) showed that J13 markedly promoted MYH9 and β-actin protein stability in HepG2 lysate and cultured HepG2 cells (Fig. 1I and G). Collectively, these findings suggest that J13 directly targeted molecular motor proteins of MYH9 and β-actin in human hepatoma cells.

3.2. *J13 suppresses MYH9—actin interaction to promote mitochondrial fission*

Since molecular motor proteins play crucial roles in mitochondrial morphology and transport, we then hypothesized that J13 may promote mitochondrial fission to exert anti-cancer effect in a MYH9-dependent manner. As shown in Fig. 2A, genetic knockdown of *MYH9* significantly reversed J13-mediated cell viability decrease. Moreover, downregulation of *MYH9* could significantly blunt J13-induced mitochondrial fission (Fig. S2D), indicating that MYH9 is of importance for J13-induced anti-cancer effects. Since MYH9—actin interaction contributes to mitochondrial dynamics, we thus explored whether J13 regulated MYH9—actin interaction. Here, co-IP assay suggested that J13 significantly inhibited MYH9 interaction with β-actin in cell lysate and recombinant proteins mixture (Fig. 2B), underlining the potential importance of MYH9—β-actin interaction in J13-mediated mitochondrial fission.

To explore the binding site of J13 to MYH9, we hypothesized that J13 influenced MYH9—actin interaction *via* actin-binding motif in MYH9. To this end, we compared the difference of J13 binding capacity with MYH9 full-length (MYH9 F) or MYH9 with actin-binding motif deletion (MYH9 M). As shown in Fig. 2C, J13 exhibited an obvious binding to MYH9 F, but a weaker interaction with MYH9 M, demonstrating that actin-binding motif was essential for J13 interaction with MYH9. Then, docking analysis showed that J13 spatially bond around actin-binding motif by forming several hydrogen bonds with arginine (ARG) 165, methionine (MET) 161, arginine (ARG) 240, lysine (LYS) 441, glycine (GLN) 443, glycine (GLY) 444, phenylalanine (PHE) 447 and asparagine (ASN) 663 (Fig. 2D). Thus, we proposed that J13 may engage the actin-binding interface in MYH9 to impair dynamical MYH9—actin interaction. Intriguingly, we observed an obvious allosteric regulation effect of J13 on MYH9 conformation change using fluorescence analysis of tryptophan (Fig. 2E), indicating that J13 may mediate MYH9 binding to β-actin *via* a putative conformational mechanism.

Since mitochondrial dynamics interferes with mitochondria-ER communication to cause ER stress, we also investigated whether J13-mediated mitochondrial dynamics imbalance impaired ER-mitochondria contact and fueled ER stress. As shown in Fig. 2F, J13 significantly suppressed ER (red)-mitochondria (green) coupling in a time-dependent manner, which was indicated by a decreasing overlap of red/green fluorescence. The reduction of ER-mitochondria contact sites may synergistically enhance J13-induced effects by inducing ER stress. To confirm whether J13-mediated mitochondrial fission contributed to ER stress, we performed MTT assays with ER stress inducers. As shown in Fig. 2G, we observed a notable synergistic inhibition effect of J13 on HepG2 cells with tunicamycin (Tu), thapsigargin (Th) and calcium ionophore III (CI), demonstrating that ER stress may be also a crucial driver for J13-dependent anti-cancer effect. Moreover, we performed MTT assay with two classic ER stress inhibitor TUDCA and 4-PBA, with or without J13, respectively. As shown in Fig. 2H, ER stress inhibitors efficiently reversed J13-induced cell viability decrease in HepG2 cells, further confirming our previous speculation that ER stress indeed is induced by J13 treatment for anti-cancer effect.

3.3. *HSPA9 is a MYH9—actin molecular motor substrate protein for controlling mitochondrial dynamics*

To explore the inter-mediators connecting MYH9—actin molecular motor to mitochondrial dynamics, we performed SILAC-based co-IP experiment to capture potential binding proteins (Fig. 3A). As shown in Fig. 3B, a 74 kDa heat-shock protein A9 (HSPA9) was identified as the most specific interacting protein of MYH9, which was confirmed by co-IP assay with specific antibodies (Fig. 3C). Immunofluorescence analysis also revealed an interesting phenomenon that J13 promoted cytoplasm translocation of HSPA9 to increase its co-location with MYH9 (Fig. 3D). Moreover, we performed cytoplasmic and nuclear fractions separation and found that HSPA9 was preferentially located in the nuclear fraction of control cells. However, upon J13 treatment, HSPA9 was considerably increased in cytosol, and thereby promoting co-location of MYH9 with HSPA9 (Fig. 3E). This observation was supported by previous reports that HSPA9 was a ubiquitously expressed mitochondrial chaperon which facilitated ER membrane interaction with mitochondrial outer membrane[29]. Then, we observed that J13 significantly decreased fluorescence intensity and disrupted fluorescence distribution of mitochondrial membrane protein cytochrome *c* oxidase subunit IV (COXIV), indicating an increase of mitochondrial fragmentation (Fig. 3F). To explore whether HSPA9 was involved in J13-meidated decrease of cell viability, HSPA9 inhibitor MKT-077 was used in our study. As shown in Fig. 3G, MKT-077 showed obvious antagonistic

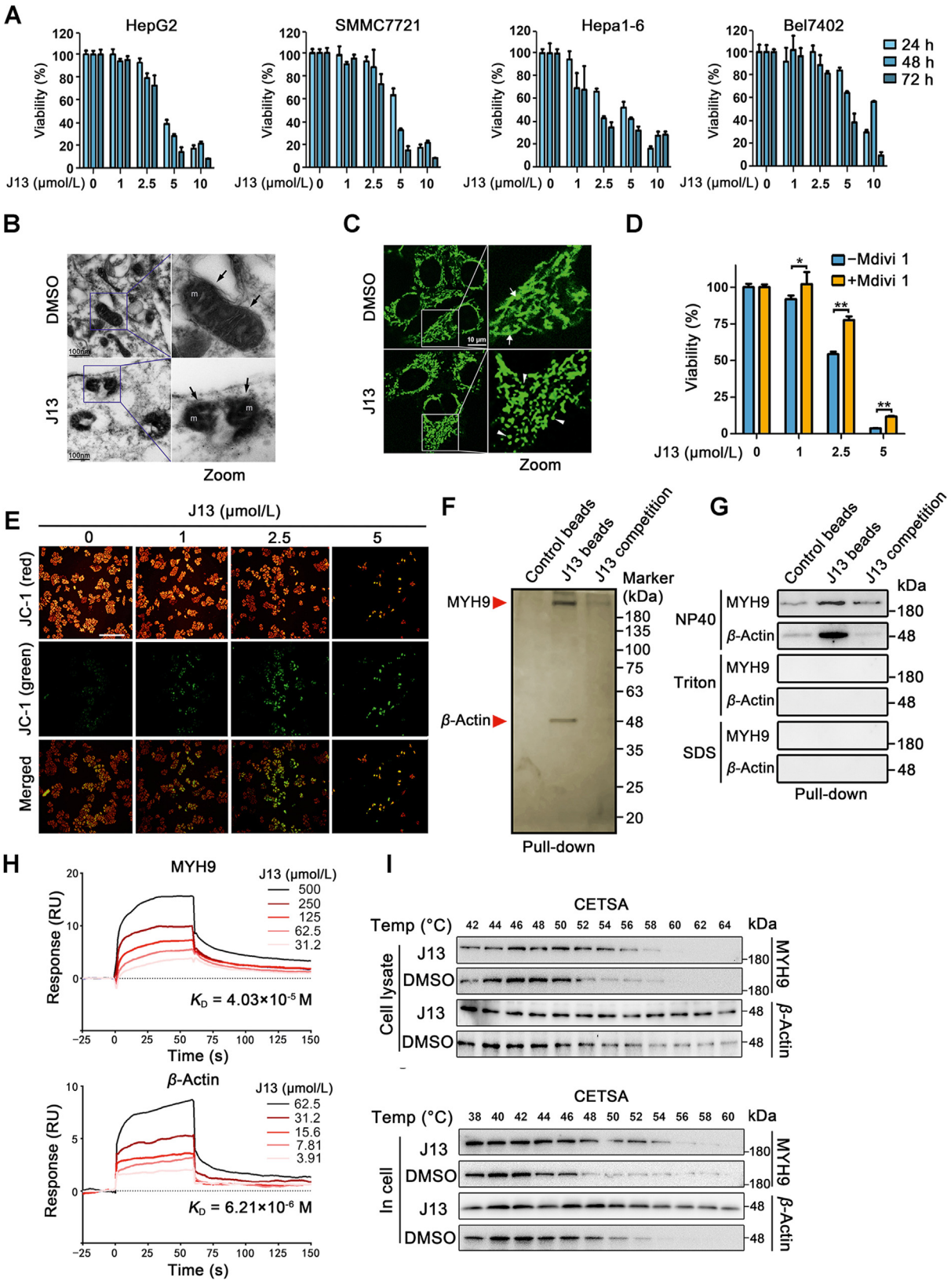

Figure 1 MYH9-actin molecular motor is a direct cellular target of anti-cancer small-molecule J13. (A) J13 inhibited cell viability of HepG2, SMMC7721, Hepa1-6 and Bel7402 cells (n = 6). (B) J13 induced mitochondrial fission in HepG2 cells. Mitochondrial morphology of HepG2 after J13 treatment was detected by transmission electron microscopy scanning (scale bar = 100 nm). (C) J13 caused mitochondrial fragmentation in HepG2 cells, which was visualized by Mito-tracker staining (scale bar = 10 μm). (D) Inhibition of mitochondrial fission by Mdivi-1 markedly reversed J13-dependent anti-cancer effects by MTT assay (n = 6). (E) J13 induced mitochondrial depolarization by JC-1 staining (scale

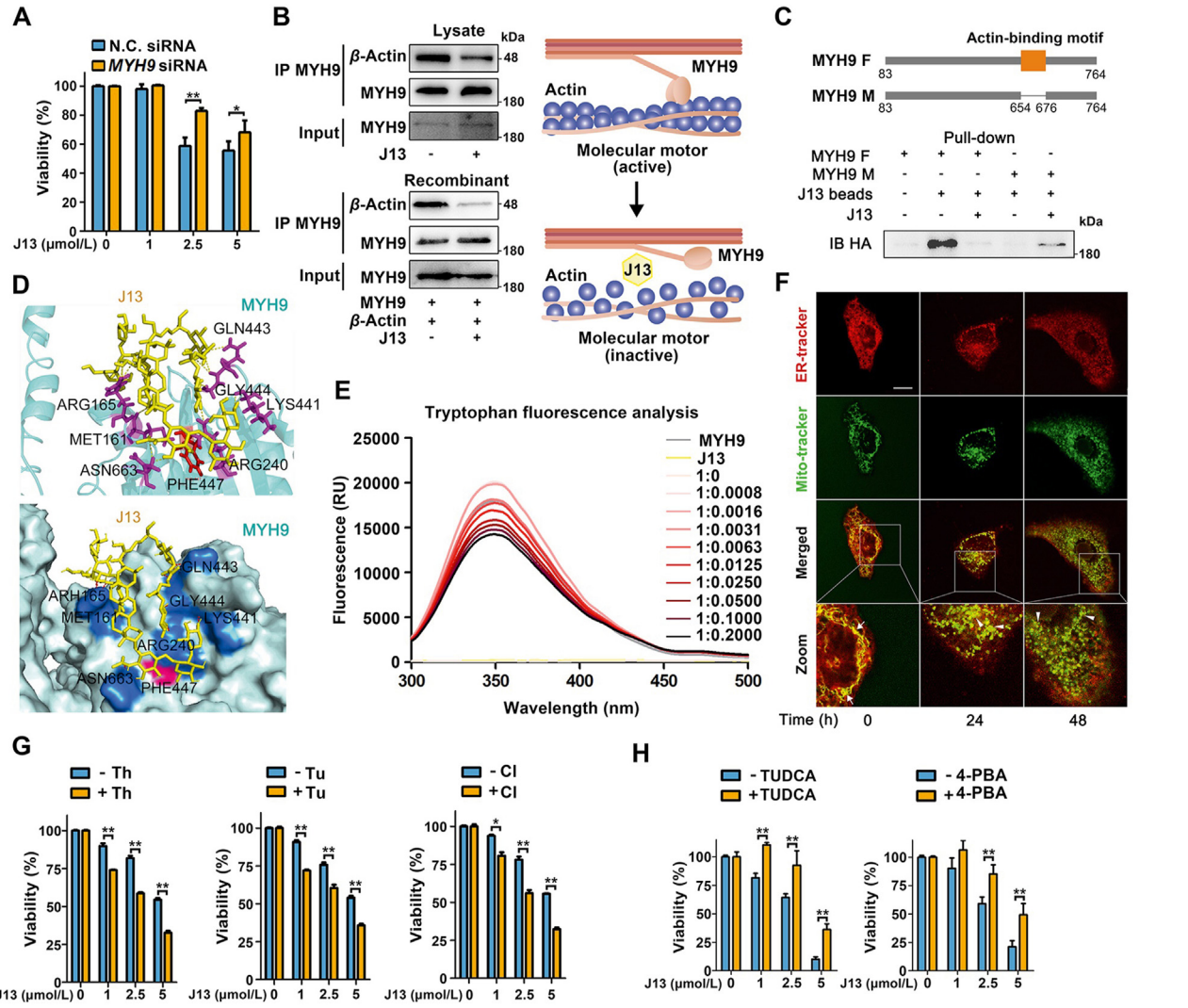

Figure 2 J13 suppresses direct MYH9−actin interaction to promote mitochondrial fission. (A) MYH9 knock-down reversed J13-dependent cell viability decrease in MTT assay. N.C.: knock-down negative control. (B) J13 suppressed the interaction of MYH9 with β-actin by co-IP assay. (C) Pull-down assay revealed that J13 interacted with actin-binding motif of MYH9. MYH9 F and M: full length MYH9 and mutated MYH9 with a deletion of 23 amino acids (654−676). (D) Docking analysis shows the amino acid residues which may form hydrogen bonds with J13 including ARG165, MET161, ARG240, LYS441, GLN443, GLY444, PHE447, and ASN663. (E) J13 induced allosteric effect of MYH9 by tryptophan fluorescence scanning analysis. (F) J13 suppressed the co-location of ER with mitochondria by double fluorescence staining analysis (ER-tracker, red; Mito-tracker, green; scale bar = 10 μm). (G) ER stress inducers including tunicamycin (Tu), thapsigargin (Th), and calcium ionophore III (CI) exacerbated J13-dependent anti-tumor effect by MTT assay. (H) ER stress inhibitor TUDCA and 4-PBA efficiently reversed J13-induced cell viability decrease in HepG2 cells. All data are presented as mean ± SD, $n = 6$; $^*P < 0.05$, $^{**}P < 0.01$.

effect against J13-mediated decrease of cell viability, suggesting that HSPA9 was a crucial signal hub in regulating MYH9−actin molecular motor-dependent cell survival. Taken together, HSPA9 may serve as a support (scaffold) or "sponge" to provide a platform for protein interactions, more precisely, inactivating the interaction between MYH9 and β-actin.

Previous reports have revealed that BCL-2 family proteins are regulated by HSPA9 for mitochondrial function control[30]. STRING analysis suggested that BCL-2 family proteins may be functionally associated with HSPA9 (Supporting Information Fig. S3A). In our study, J13 obviously increased BAX and p-BAD levels, meanwhile decreased BCL-2 and BCL-XL levels in a

bar = 25 μm). (F) MYH9 and β-actin were identified as J13-binding proteins using pull-down assay, followed by LC−MS/MS analysis with silver staining. (G) Non-covalent bindings of J13 with MYH9 or β-actin were confirmed by immunoblotting assay with different surfactants NP40, Triton, and SDS. (H) Dissociation constants (K_D) of J13 with MYH9 or β-actin were detected by surface plasmon resonance (SPR) analysis. (I) and (J) Cellular thermal shift assays (CETSA) were performed to confirm the binding specificity of J13 with MYH9 or β-actin in cell lysates and living cells. Data are presented as mean ± SD from independent experiments; $^*P < 0.05$, $^{**}P < 0.01$.

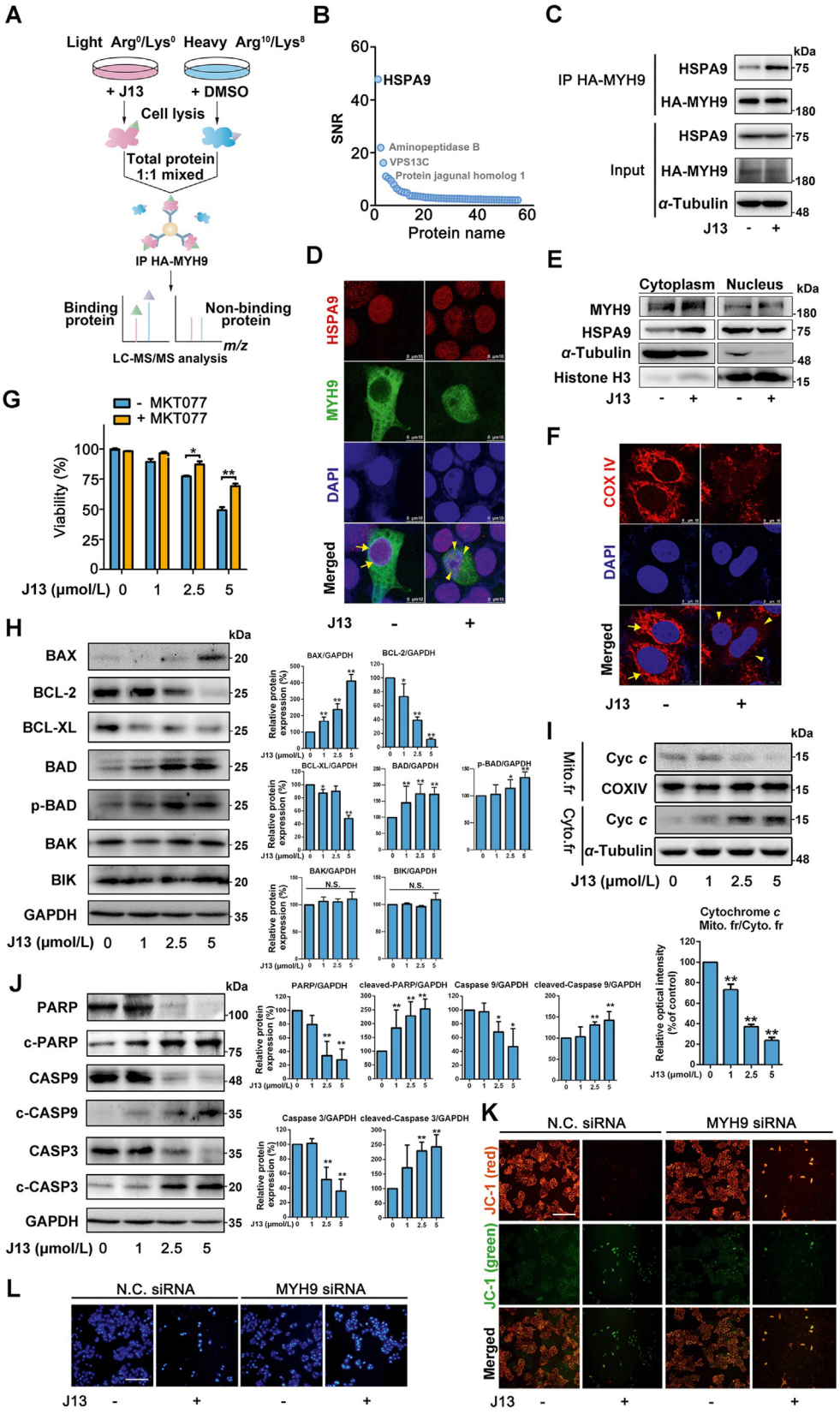

Figure 3 HSPA9 is a crucial MYH9−actin molecular motor substrate protein for controlling mitochondrial dynamics. (A) Schematic illustration of MYH9-binding proteins identification using pull-down coupled with SILAC analysis. (B) HSPA9 was identified as a binding protein of MYH9. (C) J13 promoted the interaction of HSPA9 with MYH9 by co-IP assay. (D) J13 promoted MYH9 interaction with HSPA9 in nucleus. (E) J13 treatment promoted cytosol translocation of HSPA9, and thus increased co-location of MYH9 with HSPA9. (F) J13 induced mitochondrial

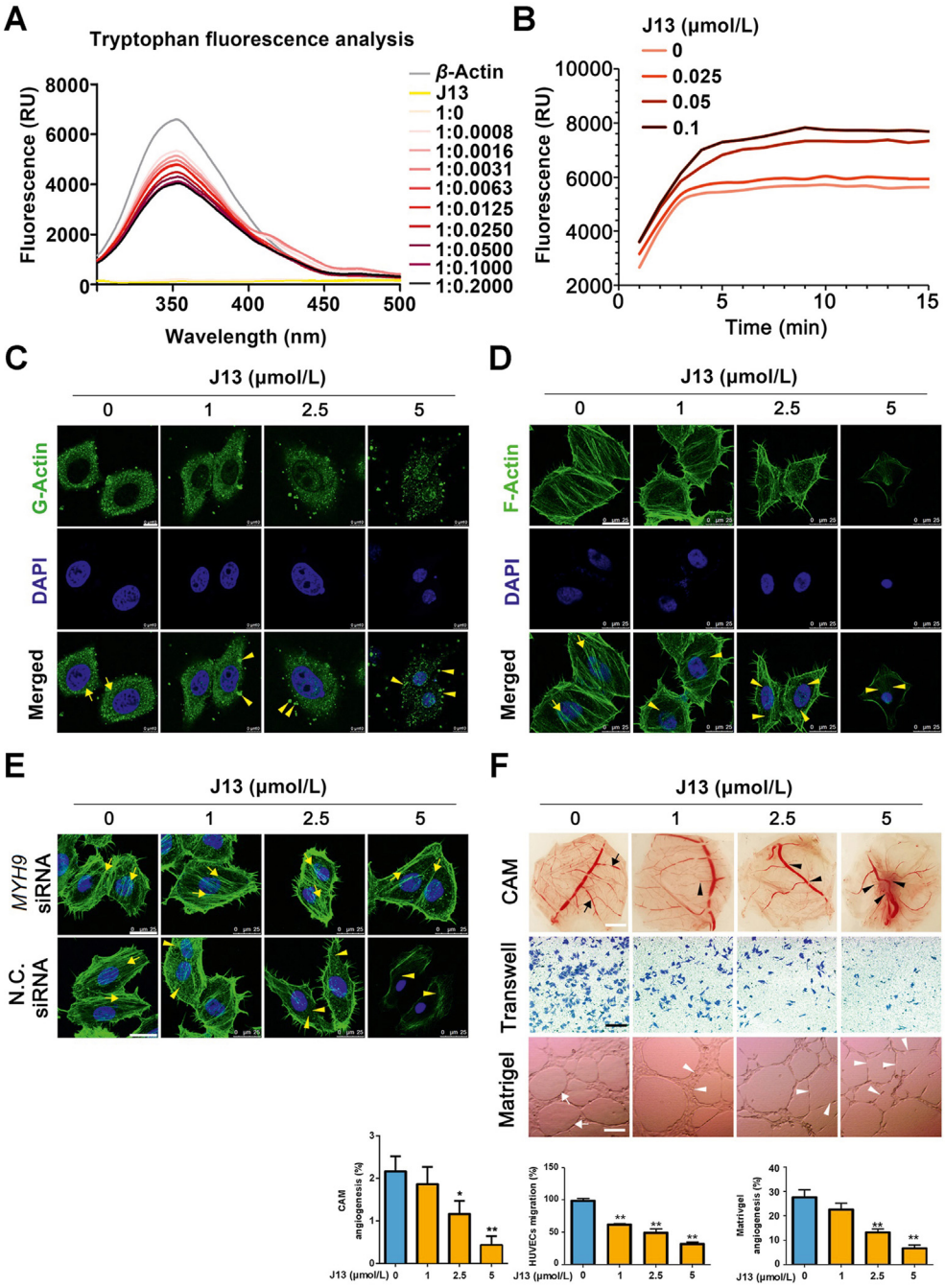

Figure 4 J13 inhibits actin-dependent cell migration and angiogenesis. (A) J13 induced allosteric effect of actin in tryptophan fluorescence scanning analysis. (B) J13 induced excessive G-actin assembly which was detected by G-actin polymerization assay. (C) J13 induced G-actin granulation aggregation in cells which was detected by immunofluorescence staining (scale bar = 10 μm). (D) J13 destroyed F-actin cytoskeleton formation which was detected by fluorescent phalloidin staining (scale bar = 25 μm). (E) MYH9 knock-down reversed J13-dependent F-actin cytoskeleton collapse (scale bar = 25 μm). (F) J13 suppressed CAM microvessels formation, cell migration and capillary-like tube formation. All data are presented as mean ± SD from independent experiments performed in triplicate. *$P < 0.05$, **$P < 0.01$.

fragmentation by disrupting COXIV fluorescence distribution. (G) HSPA9 inhibitor MKT-077 (0.5 μmol/L for 24 h) reversed J13-induced cell viability decrease by MTT assay. (H) J13 significantly induced BAX and p-BAD expressions, and inhibited BCL-2 and BCL-XL expressions. (I) J13 induced cytochrome *c* translocation from mitochondria to cytoplasm. (J) J13 activated caspase-9/3-dependent apoptosis pathway. (K) *MYH9* knock-down reversed J13-dependent mitochondrial depolarization (scale bar = 25 μm). (L) *MYH9* knock-down rescued J13-dependent cell apoptosis by Hoechst 33258 staining assay (scale bar = 25 μm). All data are presented as mean ± SD from independent experiments (G: $n = 6$, H–J: $n = 3$; *$P < 0.05$, **$P < 0.01$.

concentration-dependent manner (Fig. 3H), indicating that BCL-2 family members might be affected by J13 for mitochondrial dysfunction. This finding was also supported by the promotion effect of J13 on cytoplasm translocation of cytochrome *c* from mitochondria (Fig. 3I). Moreover, J13 induced mitochondria-dependent caspase-9/3 apoptosis pathway activation by up-regulating cleaved caspase-9/-3/PARP expressions (Fig. 3J and Fig. S3B–S3D). Next, we sought to explore whether MYH9 was a crucial determinant of mitochondrial function. Genetic knockdown of *MHY9* markedly reversed JC-1 green fluorescence (Fig. 3K), indicating that MYH9 plays a fundamental role in J13-dependent MMP decline. *MYH9* knockdown also markedly suppressed J13-mediated apoptosis in HepG2 cells (Fig. 3L). In summary, these observations suggest that HSPA9−BCL-2 family signal axis is critical to MYH9 mediated-mitochondrial dynamics for apoptosis.

3.4. J13 inhibits actin-dependent cell migration and angiogenesis

Next, we investigated whether J13 regulated the function of molecular motor protein actin. Fluorescence analysis of tryptophan revealed that the fluorescence intensity of J13−actin complex significantly decreased as J13 concentration increased, suggesting exposure and quenching of more tryptophan residues of proteins, and thus indicating an allosteric regulation effect of J13 on actin (Fig. 4A). Quantitative analysis of actin assembly dynamics showed that polymerized actin filaments rapidly formed as indicated by increasing phalloidin fluorescence after J13 treatment (Fig. 4B). Moreover, actin dynamics measurement in living cells also confirmed that monomeric G-actin was uniformly distributed in cells and formed irregular granulation aggregation upon J13 treatment (Fig. 4C). Actin-tracker for specific F-actin staining was used to explore cytoskeletal structures and result showed that J13 caused significant F-actin cytoskeletal organization collapse (Fig. 4D). Since myosin engages with F-actin to drive the alignment and compaction of F-actin cytoskeleton, we then detected whether MYH9 was involved in J13-mediated F-actin cytoskeletal organization. As shown in Fig. 4E, genetic *MYH9* knockdown reversed J13-dependent F-actin cytoskeletal collapse, indicating a crucial role of MYH9 in J13-mediated F-actin cytoskeletal organization.

Actin filaments are responsible for diversified cell functions including cell migration and angiogenesis. Therefore, we investigated whether J13 mediated vascular endothelial cells (HUVECs) migration using matrigel-coated Transwell chambers. As shown in Fig. 4F, J13 strikingly suppressed HUVECs migration and impaired the formation of capillary-like tube structures of HUVECs on matrigel. Furthermore, J13 markedly inhibited neovascularization in chicken embryo chorioallantoic membrane

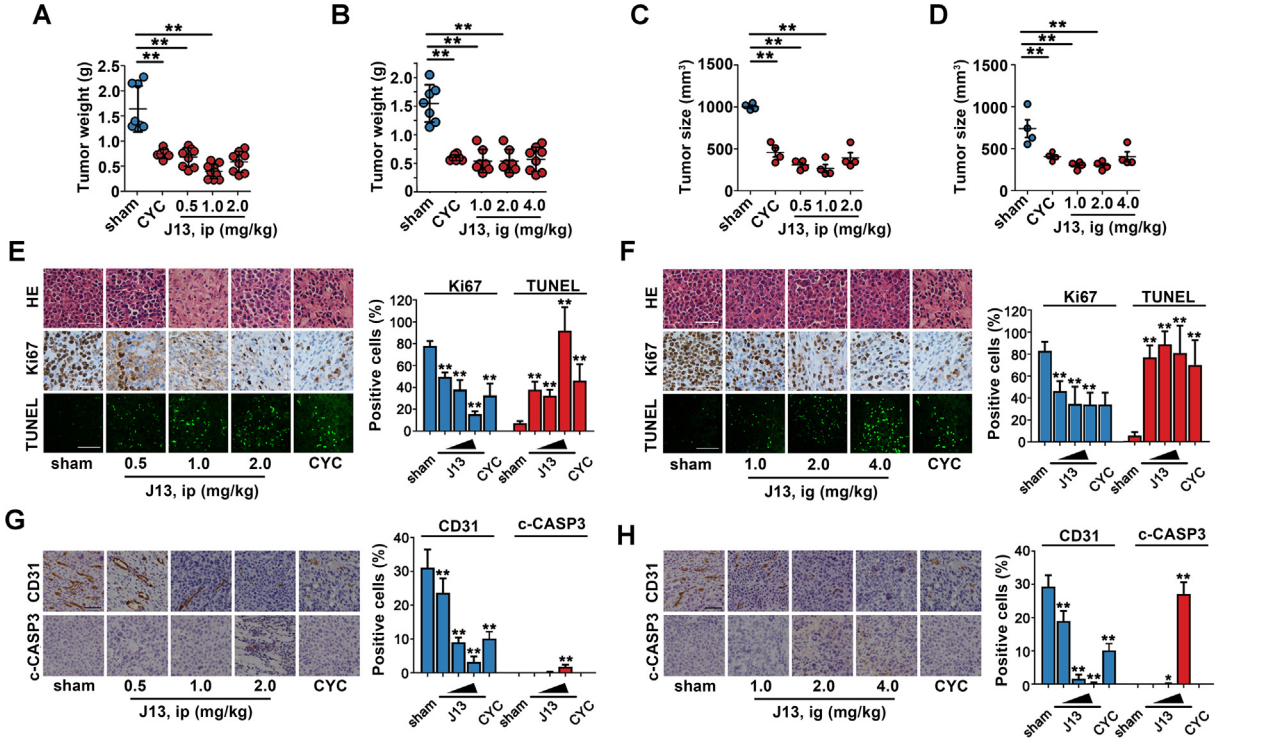

Figure 5 J13 showed anti-tumor effects *in vivo*. (A) J13 inhibited liver tumor weight growth in H22-bearing ICR mice *in vivo* by intraperitoneal injection (ip). (B) J13 inhibited liver tumor weight growth of H22-bearing ICR mice *in vivo* by intragastric administration (ig). (C) J13 inhibited liver tumor size in H22-bearing ICR mice *in vivo* by intraperitoneal injection (ip). (D) J13 inhibited liver tumor size of H22-bearing ICR mice *in vivo* by intragastric administration (ig). (E) J13 destroyed cell structure by HE staining (scale bar = 50 μm), decreased Ki67-positive cells number (scale bar = 50 μm), and promoted TUNEL-positive cell apoptosis (scale bar = 20 μm) by ip. (F) J13 destroyed cell structure by HE staining, decreased Ki67-positive cells number, and promoted TUNEL-positive cell apoptosis (scale bar = 20 μm) by ig. (G) J13 reduced CD31-positive cells number and promoted cleaved-caspase 3 (c-CASP3) expression (scale bar = 50 μm) by ip. (H) J13 reduced CD31-positive cells number and promoted c-CASP3 expression (scale bar = 50 μm) by ig. All data are presented as mean ± SD from independent experiments (A–D: $n \geq 8$, E–H: $n = 3$); *$P < 0.05$, **$P < 0.01$.

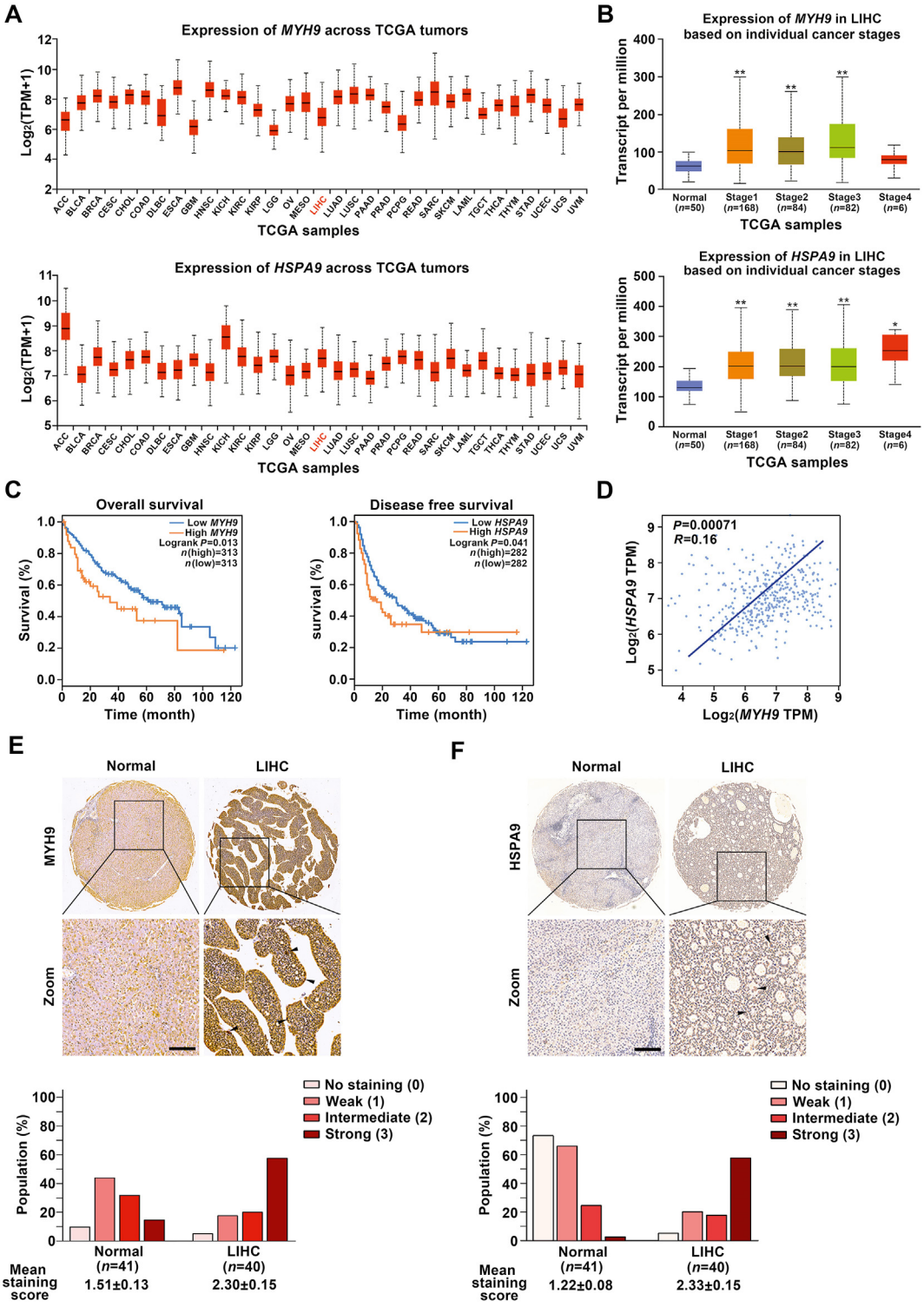

Figure 6 *MYH9* and *HSPA9* expressions are highly associated with poor survival of liver hepatocellular carcinoma (LIHC) patients. (A) *MYH9* and *HSPA9* had high expression levels in a variety of malignancies [Log_2 (TPM+1) $\geq$2], including liver hepatocellular carcinoma LIHC from TCGA database. (B) The expression levels of *MYH9/HSPA9* in LIHC were positively associated with advanced tumor stage determined by TCGA database. (C) *MYH9* expression was positively correlated with LIHC patient overall survival ($P = 0.013$), while *HSPA9* expression was positively related with disease free survival of LIHC patients ($P = 0.041$) based on GEPIA database. (D) A correlation between *MYH9* and *HSPA9* mRNA expression levels was shown by scatter plot ($P = 0.00071$) based on two-tailed Pearson's correlation analysis. (E) and (F) The expression levels of MYH9/HSPA9 were markedly increased in LIHC tissues ($n = 40$) compared to adjacent normal tissues ($n = 41$), as shown in representative immunohistochemical images (scale bar = 100 μm) and mean staining scores ($P < 0.001$, nonparametric ANOVA). *$P < 0.05$, **$P < 0.01$.

(CAM, Fig. 4F). Taken together, these data indicate that J13 affected actin cytoskeletal structures to inhibit cell migration and angiogenesis.

3.5. *J13 showed anti-tumor effects in vivo*

We further investigated the effect of J13 on tumor growth of mouse H22 hepatocarcinoma cells-bearing mice. As shown in Fig. 5A−D, both intraperitoneal injection and intragastric administration of J13 induced significant tumor regression, without obvious immunosuppressive side effects (Supporting Information Fig. S4). Further pathological examinations including HE, Ki67 IHC and TUNEL staining revealed that J13 effectively destroyed cell structure, reduced Ki67 positive cells number, and promoted TUNEL-positive cells increase in tumor tissues (Fig. 5E and F). Moreover, J13 significantly decreased CD31 and increased cleaved caspase-3 (c-CASP3) expressions in tumors of xenograft model, indicating that J13 effectively inhibited tumor angiogenesis and activated tumor apoptosis *in vivo* (Fig. 5G and H). To sum up, J13 exhibited an obvious anti-tumor effect *in vivo* through suppression of tumor proliferation and angiogenesis as well as induction of tumor cell apoptosis.

3.6. *MYH9 and HSPA9 expressions are highly associated with poor survival of liver hepatocellular carcinoma (LIHC) patients*

To further clarify the relationship between MYH9/HSPA9 expressions and LIHC, we analyzed clinical samples from TCGA and GTEx databases which are widely used in oncology research[31,32]. According to TCGA database, *MYH9* and *HSPA9* showed high expressions in a variety of malignancies, including LIHC [$Log_2(TPM+1)\geq 2$; Fig. 6A]. Additionally, *HSPA9* expression was positively associated with advanced tumor stage, especially for the patients with stage 4. Meanwhile, high expression of *MYH9* was significantly related with LIHC patients with stages I to III (Fig. 6B and Supporting Information Fig. S5A). Moreover, *MYH9* and *HSPA9* were found to be closely associated with the prognosis of LIHC patients. As shown in Fig. 6C, the patients with high *MYH9* expression had poor overall survival; meanwhile, those with high *HSPA9* expression showed shorter disease free survival. Furthermore, we analyzed the correlation of *MYH9* and *HSPA9* mRNA expressions, and found *MYH9* was positively correlated with *HSPA9* (Pearson correlation coefficient, $P = 0.00071$; Fig. 6D). Patient tissue biopsy specimens of LIHC also supported that MYH9 and HSPA9 had high expression levels in LIHC tissues compared with adjacent normal tissues (Fig. 6E and F). Taken together, these results suggest that MYH9 and HSPA9 are highly associated with LIHC progression, and can be used as prognostic biomarkers for the disease.

4. Discussion

Albizia julibrissin, also called mimosa or Persian silktree, is a member of the family Leguminosae. Albizziae cortex (AC), the stem bark of *Albizia julibrissin*, has been widely used for the treatment of insomnia in traditional Chinese medicine as a sedative and anti-inflammatory agent[33]. It has also been used as a vital composition of clinical anti-tumor prescriptions[34−36]. Previous studies have reported that the chemical compositions of AC include saponins, flavonoids, alkaloids and polysaccharides. Of note, triterpenoid saponins are considered to be the major anti-tumor components[37−40]. Julibroside J13 was one of the most abundant saponin components in AC, and has been identified by our laboratory[41]. The molecular structure of J13 promotes it to be a suitable lead compound for anti-cancer reagents development. However, the underlying anti-cancer mechanisms still remain to be elucidated.

In this study, we used J13 as a molecule probe to explore the anti-hepatoma carcinoma targets. Particularly, we deeply investigated the regulatory mechanism of J13 on target proteins function and associated molecular signaling pathways. Therefore, J13 may serve as a lead compound for further drug development by activity improvement *via* structural modification.

Despite accumulating studies on mitochondrial fission/fusion in cancer pathological processes, little is known about potential therapeutic target proteins for mitochondrial dynamics modulation[17,42]. Myosin is actin-based molecular motor protein using ATP energy to maintain mitochondrial dynamics. Interaction of myosin with actin effectively powers mitochondrial fission/fusion process to drive cancer cells division, proliferation, and motility[43]. Thus, targeting myosin−actin molecular motor may be a potential strategy for anti-cancer[44]. However, until nowadays, this hypothesis has not been well explored for its pharmacological application in cancer therapeutics. Thus, we performed a proof-of-concept investigation with natural small-molecule J13, and revealed that myosin−actin molecular motor can be used as a druggable target for anti-cancer effects.

Alterations in mitochondrial dynamics due to chemical regulations may advance the development of novel anti-cancer strategy[45]. However, there has been lack of precise and reliable chemical agents to effectively modulate mitochondrial fission/fusion dynamics[46]. Our finding has provided important clues that mitochondrial dynamics can be regulated by targeting myosin−actin molecular motor using a small-molecule J13. Thus, J13 may represent the first small-molecule lead compound targeting myosin−actin molecular motor for further candidate drug structure optimization and structure-guided anti-cancer drug design. Curiously, previous reports have suggested that contacts between mitochondria and ER are vital for ER homeostasis[47]. Meanwhile, ER wraps around mitochondria and regulates mitochondrial constriction at ER−mitochondria contact sites. In this study, we observed that J13 caused mitochondrial fission by inhibiting MYH9−actin interaction, and disturbed ER−mitochondria contacts which resulted in ER stress. Thus, our observation provides a promising avenue for therapeutic interventions for anti-cancer by synergistically using molecular motor-targeting molecules with ER regulators.

As a highly conserved heat-shock chaperone, HSPA9 possesses several binding partners with multiple biological functions especially for cell stress. HSPA9 is also involved in various human diseases including cancers, Alzheimer's disease and Parkinson's disease[48,49]. Here, HSPA9 was identified as a substrate protein of MYH9. Further study showed HSPA9 was a crucial functional linker of molecular motor and mitochondrial fission. Meanwhile, HSPA9 has previously been found to regulate BCL-2 family protein expressions to modulate mitochondrial homeostasis[50]. Therefore, HSPA9−BCL-2 family signal is a key molecular pathway for controlling mitochondrial function. Here, we observed that J13 induced an obvious cytoplasm translocation of HSPA9 and overlapped with MYH9. Although there still lacks enough evidence, we tend to speculate that MYH9 might interact with HSPA9 and impair HSPA9−P53 interaction, further disturbing P53-dependant transcriptional regulation and BCL-2

family gene expressions in cancer cells. Of course, this needs further investigation.

Mitochondrial morphologies are dynamically changed between fission/fusion balances and highly associated with mitochondrial 'health' status[6]. Therefore, mitochondrial fission/fusion dynamics contributes to mitochondrial quality control[51,52]. We propose that J13 induced mitochondrial fission to cause mitochondrial membrane potential (MMP) decrease and resultant caspase-dependent apoptosis signal activation. Notably, genetic knockdown of *MYH9* reversed J13-dependent MMP decrease, indicating MYH9 is a key regulator for controlling mitochondrial quality as well as homeostasis. One possible mechanism may be that J13 impaired mitochondrial dynamics by targeting MYH9, and inhibited mitochondrial self-renewal by excessively promoting its fission process. Meanwhile, J13 may also mediate MYH9−HSPA9−BCL-2 family signal axis to induce BAX/p-BAD increase and BCL-2/BCL-XL downregulation. Since previous reports have revealed that HSPA9 is closely associated with P53, RAF/MEK, and HIF-1α[53,54], thus we speculate these interactions can regulate mitochondria-related genes expression for maintaining MMP and mitochondrial function.

We note that J13 also showed direct actin-binding effect to regulate actin dynamics, contributing to a great number of cellular processes including cell polarity, morphogenesis, and motility. This indicates that J13 may regulate myosin−actin molecular motor function by targeting multiple players on molecular motor. Moreover, actin filaments are polarized polymers in conjunction with myosin, and myosin movement along actin filaments correlates with mitochondrial fission/fusion dynamics[55]. Thus we speculate that J13 may promote mitochondrial fission by targeting actin filaments and impair myosin movement. Meanwhile, mitochondria migrate along protein filaments to different cellular locations with energy demands[56]. Our data suggest that J13 markedly affected mitochondrial distribution in cells, hinting that mitochondria attachment to protein filaments may be strictly regulated by pharmacological targeting filament proteins[57].

Mitochondrial fission/fusion imbalance is well documented in LIHC; however, treatment strategies for LIHC by targeting mitochondrial fission/fusion dynamics still remain unclear. In this study, based on bioinformatics and immunohistochemical analysis of clinical samples, we found that MYH9/HSPA9 expressions were significantly upregulated in LIHC tissues, which could be considered as independent prognostic factors for LIHC patient survival. Unexpectedly, HSPA9 expression was barely related with LIHC patient overall survival. We speculate that there is a loss of LIHC patients to follow-up by 40th month. Thus, we analyzed the relationship between HSPA9 expression and disease free survival, which is widely used as an early surrogate endpoint for overall survival[58]. Moreover, a positive correlation between MYH9 and HSPA9 levels in LIHC indicated that MYH9/HSPA9 may be regulated in the same signaling pathway. In that scenario, combination therapy of MYH9- and HSPA9-inhibitors may synergistically improve cancer outcomes. Collectively, these data indicate that MYH9 and HSPA9 are positively correlated with LIHC progression, which is of clinical significance for the diagnosis and management of LIHC.

5. Conclusions

Taken together, we identified the first small-molecule J13 which can directly target myosin−actin molecular motor to promote mitochondrial fission for cancer therapy. Therefore, our study puts forward a conceptual framework for novel anti-cancer strategy of pharmacologically regulating mitochondrial dynamics by targeting myosin−actin molecular motor.

Acknowledgments

This study was supported by the National Key Technology R&D Program "New Drug Innovation" of China [Nos. 2019YFC1711000 and 2019YFC1708902] and the National Natural Science Foundation of China [Nos. 81973505 and 81773932].

Author contributions

Kewu Zeng and Hong Liang designed the project. Yi Qian and Meimei Zhao performed most of the experiments and analyzed data. Qinghua Han performed *in vivo* experiments. Jingkang Wang, Lixi Liao and Heng Yang performed the molecular biology and cell biology experiments. Dan Liu performed MS analysis. Kewu Zeng, Yi Qian and Meimei Zhao wrote the manuscript. Pengfei Tu contributed to the manuscript editing. All authors contributed and approved the final version of the manuscript.

Conflicts of interest

The authors declare that there are no competing interests.

Appendix A. Supporting information

Supporting data to this article can be found online at https://doi.org/10.1016/j.apsb.2021.01.011.

References

1. Chan DC. Mitochondria: dynamic organelles in disease, aging, and development. *Cell* 2006;**125**:1241−52.
2. Schapira AH. Mitochondrial diseases. *Lancet* 2012;**379**:1825−34.
3. Wei MC, Zong WX, Cheng EH, Lindsten T, Panoutsakopoulou V, Ross AJ, et al. Proapoptotic BAX and BAK: a requisite gateway to mitochondrial dysfunction and death. *Science* 2001;**292**:727−30.
4. Lin MT, Beal MF. Mitochondrial dysfunction and oxidative stress in neurodegenerative diseases. *Nature* 2006;**443**:787−95.
5. Liesa M, Palacin M, Zorzano A. Mitochondrial dynamics in mammalian health and disease. *Physiol Rev* 2009;**89**:799−845.
6. Chan DC. Fusion and fission: interlinked processes critical for mitochondrial health. *Annu Rev Genet* 2012;**46**:265−87.
7. Sabouny R, Shutt TE. Reciprocal regulation of mitochondrial fission and fusion. *Trends Biochem Sci* 2020;**4**:564−77.
8. Liesa M, Shirihai OS. Mitochondrial dynamics in the regulation of nutrient utilization and energy expenditure. *Cell Metabol* 2013;**17**:491−506.
9. Fabian SG, Frederic D. Mitochondrial fission and fusion in human diseases. *N Engl J Med* 2014;**370**:1073−4.
10. Vyas S, Zaganjor E, Haigis MC. Mitochondria and cancer. *Cell* 2016;**166**:555−66.
11. Kashatus JA, Nascimento A, Myers LJ, Sher A, Byrne FL, Hoehn KL, et al. Erk2 phosphorylation of Drp1 promotes mitochondrial fission and MAPK-driven tumor growth. *Mol Cell* 2015;**57**:537−51.
12. Serasinghe MN, Wieder SY, Renault TT, Elkholi R, Asciolla JJ, Yao JL, et al. Mitochondrial division is requisite to RAS-induced transformation and targeted by oncogenic MAPK pathway inhibitors. *Mol Cell* 2015;**57**:521−36.
13. Chen H, Chan DC. Mitochondrial dynamics in regulating the unique phenotypes of cancer and stem cells. *Cell Metabol* 2017;**26**:39−48.

14. Srinivasan S, Guha M, Kashina A, Avadhani NG. Mitochondrial dysfunction and mitochondrial dynamics—the cancer connection. *Biochim Biophys Acta Bioenerg* 2017;**1858**:602−14.
15. Nagdas S, Kashatus JA, Nascimento A, Hussain SS, Trainor RE, Pollock SR, et al. Drp1 promotes KRas-driven metabolic changes to drive pancreatic tumor growth. *Cell Rep* 2019;**28**:1845−59.
16. Seo JH, Agarwal E, Chae YC, Lee YG, Garlick DS, Storaci AM, et al. Mitochondrial fission factor is a novel Myc-dependent regulator of mitochondrial permeability in cancer. *EbioMedicine* 2019;**48**: 353−63.
17. Senft D, Ronai ZA. Regulators of mitochondrial dynamics in cancer. *Curr Opin Cell Biol* 2016;**39**:43−52.
18. Cao J, Wei R, Yao S. Matrine has pro-apoptotic effects on liver cancer by triggering mitochondrial fission and activating Mst1-JNK signaling pathways. *J Physiol Sci* 2019;**69**:185−98.
19. Tiku V, Tan MW, Dikic I. Mitochondrial functions in infection and immunity. *Trends Cell Biol* 2020;**30**:263−75.
20. Detmer SA, Chan DC. Functions and dysfunctions of mitochondrial dynamics. *Nat Rev Mol Cell Biol* 2007;**8**:870−9.
21. Molloy JE, Veigel C. Biophysics. Myosin motors walk the walk. *Science* 2003;**300**:2045−6.
22. Kruppa AJ, Itakura CK, Masters TA, Rorbach JE, Grice GL, Jones JK, et al. Myosin VI-dependent actin cages encapsulate parkin-positive damaged mitochondria. *Dev Cell* 2018;**44**:484−99.
23. Yang C, Svitkina TM. Ultrastructure and dynamics of the actin−myosin II cytoskeleton during mitochondrial fission. *Nat Cell Biol* 2019;**21**:603−13.
24. Korobova F, Gauvin TJ, Higgs HN. A role for myosin II in mammalian mitochondrial fission. *Curr Biol* 2014;**24**:409−14.
25. Korobova F, Ramabhadran V, Higgs HN. An actin-dependent step in mitochondrial fission mediated by the ER-associated formin INF2. *Science* 2013;**339**:464−7.
26. Honrath B, Metz I, Bendridi N, Rieusset J, Culmsee C, Dolga AM. Glucose-regulated protein 75 determines ER−mitochondrial coupling and sensitivity to oxidative stress in neuronal cells. *Cell Death Discovery* 2017;**3**:e17076.
27. Han Q, Qian Y, Wang X, Zhang Q, Cui J, Tu P, et al. Cytotoxic oleanane triterpenoid saponins from *Albizia julibrissin*. *Fitoterapia* 2017;**121**:183−93.
28. Liao LX, Song XM, Wang LC, Lv HN, Chen JF, Liu D, et al. Highly selective inhibition of IMPDH2 provides the basis of antineuroinflammation therapy. *Proc Natl Acad Sci U S A* 2017;**114**:5986−94.
29. Starenki D, Hong SK, Lloyd RV, Park JI. Mortalin (GRP75/HSPA9) upregulation promotes survival and proliferation of medullary thyroid carcinoma cells. *Oncogene* 2015;**34**:4624−34.
30. Tang Z, Kang B, Li C, Chen T, Zhang Z. GEPIA2: an enhanced web server for large-scale expression profiling and interactive analysis. *Nucleic Acids Res* 2019;**47**:556−60.
31. Consortium GT. The genotype-tissue expression (GTEx) project. *Nat Genet* 2013;**45**:580−5.
32. Anderson GR, Wardell SE, Cakir M, Yip C, Ahn YR, Ali M, et al. Dysregulation of mitochondrial dynamics proteins are a targetable feature of human tumors. *Nat Commun* 2018;**9**:e1677.
33. He Y, Wang Q, Ye Y, Liu Z, Sun H. The ethnopharmacology, phytochemistry, pharmacology and toxicology of genus *Albizia*: a review. *J Ethnopharmacol* 2020;**257**:e112677.
34. Feng L, Tan Y, Qiu LY, Gu XT, Zhou XZ. Optimizing extraction process for Yiyuan Yiliu decoction by orthogonal design using multi-index. *Chin J Hosp Pharm* 2013;**33**:601−4.
35. Tan Y, Qiu LY, Mao HY, Zhou XZ, Feng L. Study on formation process of "Yiyuan Yiliu Tang" granules. *Chin Tradit Pat Med* 2013; **35**:2050−3.
36. Yi QQ, Tan Y, Li R, Du B, Feng L, Qiu LY. Investigation of immunity capability of "Yiyuan Yiliu Tang" in H 22 tumor-burdened mice. *Chin J Immunol* 2014;**30**:205−8.
37. Zhang L, Zheng J, Wu LJ, Zhao YY. Julibroside J8-induced HeLa cell apoptosis through caspase pathway. *J Asian Nat Prod Res* 2006;**8**: 457−65.
38. Qian Y, Han QH, Wang LC, Guo Q, Wang XD, Tu PF, et al. Total saponins of Albiziae Cortex show anti-hepatoma carcinoma effects by inducing S phase arrest and mitochondrial apoptosis pathway activation. *J Ethnopharmacol* 2018;**221**:20−9.
39. Yu DH, Qiao SY, Zhao YM. Advances in study on bark of *Albizzia julibrissin*. *China J Chin Mater Med* 2004;**29**:619−24.
40. Hua H, Feng L, Zhang XP, Zhang LF, Jin J. Anti-angiogenic activity of julibroside J8, a natural product isolated from *Albizia julibrissin*. *Phytomedicine* 2009;**16**:703−11.
41. Zou K, Tong WY, Liang H, Cui JR, Tu GZ, Zhao YY, et al. Diastereoisomeric saponins from *Albizia julibrissin*. *Carbohydr Res* 2005; **340**:1329−34.
42. Muller M, Diensthuber RP, Chizhov I, Claus P, Heissler SM, Preller M, et al. Distinct functional interactions between actin isoforms and nonsarcomeric myosins. *PLoS One* 2013;**8**:e70636.
43. Makowska KA, Hughes RE, White KJ, Wells CM, Peckham M. Specific myosins control actin organization, cell morphology, and migration in prostate cancer cells. *Cell Rep* 2015;**13**:2118−25.
44. Yang X, Dong QF, Li LW, Huo JL, Li PQ, Fei Z, et al. The cap-translation inhibitor 4EGI-1 induces mitochondrial dysfunction *via* regulation of mitochondrial dynamic proteins in human glioma U251 cells. *Neurochem Int* 2015;**90**:98−106.
45. Franco A, Kitsis RN, Fleischer JA, Gavathiotis E, Kornfeld OS, Gong G, et al. Correcting mitochondrial fusion by manipulating mitofusin conformations. *Nature* 2016;**540**:74−9.
46. Erpapazoglou Z, Liger FM, Corti O. From dysfunctional endoplasmic reticulum−mitochondria coupling to neurodegeneration. *Neurochem Int* 2017;**109**:171−83.
47. Wu PK, Hong SK, Park JI. Steady-state levels of phosphorylated mitogen-activated protein kinase kinase 1/2 determined by mortalin/HSPA9 and protein phosphatase 1 alpha in KRAS and BRAF tumor cells. *Mol Cell Biol* 2017;**37**. e00061-17.
48. Park SJ, Shin JH, Jeong JI, Sone JH, Jo YK, Kim ES, et al. Down-regulation of mortalin exacerbates Abeta-mediated mitochondrial fragmentation and dysfunction. *J Biol Chem* 2014;**289**:2195−204.
49. Vander Heiden MG, Thompson CB. Bcl-2 proteins: regulators of apoptosis or of mitochondrial homeostasis?. *Nat Cell Biol* 1999;**1**:209−16.
50. Mishra P, Chan DC. Mitochondrial dynamics and inheritance during cell division, development and disease. *Nat Rev Mol Cell Biol* 2014; **15**:634−46.
51. Westermann B. Mitochondrial fusion and fission in cell life and death. *Nat Rev Mol Cell Biol* 2010;**11**:872−84.
52. Wu PK, Hong SK, Veeranki S, Karkhanis M, Starenki D, Plaza JA, et al. A mortalin/HSPA9-mediated switch in tumor-suppressive signaling of Raf/MEK/extracellular signal-regulated kinase. *Mol Cell Biol* 2013;**33**:4051−67.
53. Sane S, Abdullah A, Boudreau DA, Autenried RK, Gupta BK, Wang X, et al. Ubiquitin-like (UBX)-domain-containing protein, UBXN2A, promotes cell death by interfering with the p53-Mortalin interactions in colon cancer cells. *Cell Death Dis* 2014;**5**:e1118.
54. Altmann K, Frank M, Neumann D, Jakobs S, Westermann B. The class V myosin motor protein, Myo2, plays a major role in mitochondrial motility in *Saccharomyces cerevisiae*. *J Cell Biol* 2008;**181**:119−30.
55. Hatch AL, Gurel PS, Higgs HN. Novel roles for actin in mitochondrial fission. *J Cell Sci* 2014;**127**:4549−60.
56. Boldogh IR, Pon LA. Mitochondria on the move. *Trends Cell Biol* 2007;**17**:502−10.
57. Boldogh IR, Pon LA. Interactions of mitochondria with the actin cytoskeleton. *Biochim Biophys Acta* 2006;**1763**:450−62.
58. Kemp R, Prasad V. Surrogate endpoints in oncology: when are they acceptable for regulatory and clinical decisions, and are they currently overused?. *BMC Med* 2017;**15**:e134.